

Finite Element Comparison of Homogenous Ridged and Non-Ridged X-Band Rectangular Waveguide Dispersion Characteristics

Samuel J. Wyss[†]

[†]School of Nuclear Engineering
Purdue University
West Lafayette, Indiana 47907
E-mail: wysss@purdue.edu

Abstract—Two dimensional Finite Element Analysis (FEA) is applied to assess dispersion characteristics of homogenous rectangular, circular and ridged rectangular X-Band waveguides. To model these systems *in silico*, the weak form of the wave equation is derived from Maxwell's Equations for both TE and TM modes. Perfect electrical conductors (PECs) are used as waveguide walls as to neglect the effect of wave leakage into the environment. The model is validated against the analytical dispersion curves for homogenous rectangular waveguides. Dispersion characteristics of circular waveguides are assessed. A comparison of dispersion characteristics for ridged and non-ridged rectangular waveguides is provided which is then used to assess real world applications of ridged waveguides.

I. INTRODUCTION

Waveguides are used in a plethora of applications ranging from transmitting microwave fields to acting as passive, low-pass filters [1]. While any cross section of a single conductor waveguide can support TE and TM modes, rectangular and circular cross sections are commonly chosen due to their ease of construction and analytic propagation characteristics. However, a limitation of rectangular waveguides is the limited bandwidth of their dominant mode which is less than an octave [1]. By adding a single or double ridge to the mouth of a waveguide, the cutoff frequency of the dominant mode can be reduced thus allowing for increased signal bandwidth [1]. This increased bandwidth comes at the cost of reduced power capacity due to the reduction in breakdown potential between the ridges [1] making them less ideal for High Power Microwave (HPM) devices.

All wave phenomenon in an arbitrarily shaped, infinitely long waveguide at a given frequency are governed by the frequency domain Maxwell's Equations. Of these equations, Faraday's and Ampère's laws, can be manipulated to create Helmholtz wave equations which capture nearly all electromagnetic wave phenomenon to a high degree of accuracy [2]. The Finite Element Method (FEM) converges on the analytic solution of the wave equation by approximating a weak form of the Helmholtz equations over a finite set of elements within the simulation domain using weighted residuals. To convert the full wave equation to its weak form, the Galerkin method is employed for which the weighting functions are

identical to continuous basis functions as is common in Computational Electromagnetics (CEM) Finite Element Analysis (FEA) [2]. In the case of an arbitrarily shaped, infinitely long waveguide, the full-field, frequency-domain solutions can be obtained by solving for the fields in a cross sectional slice of the waveguide. FEM operates on non-uniform, conformal meshes which allows for arbitrary waveguide cross sections to be modeled without stairstepping error unlike that of the structured meshes of Finite-Difference Time-Domain (FDTD). In addition to this, FEM allows for full three dimensional solutions of such a waveguide to be obtained by only solving for a representative two dimensional slice making FEM an ideal choice for analyzing homogenous waveguides.

The development and results of this work are laid out as follows. Section II contains derivations of the Galerkin weak forms of the Helmholtz wave equations for both the TE and TM modes as well as the formation of the FEM matrices via the assembly process. Section III contains a verification of the model with analytic data for a square waveguide, an analysis and discussion of propagation in circular waveguides, as well as a comparison of rectangular waveguides to their ridged counterparts. Finally, Section IV contains closing remarks regarding the analysis and potential future work.

II. MATHEMATICAL MODEL

To model these systems *in silico*, an appropriate mathematical model must first be derived from Maxwell's Equations. The development of said model is arranged as follows. Section II-1 contains the derivation of the Helmholtz wave equations and corresponding boundary conditions from Maxwell's Equations. Section II-2 consists of the derivation of the Galerkin weak form of both Helmholtz wave equations. Section II-3 outlines the FEM assembly method using analytical forms of integrals derived in II-2.

1) *Governing Equations*: The frequency domain Maxwell's Equations in the absence of electric or fictitious magnetic currents are,

$$\nabla \times \mathbf{E} = -j\omega\mathbf{B}, \quad (1)$$

and

$$\nabla \times \mathbf{H} = -j\omega\mathbf{D} \quad (2)$$

where \mathbf{E} is the electric field intensity, \mathbf{B} is the magnetic flux density, \mathbf{H} is the magnetic field intensity, and \mathbf{D} is the electric flux density.

For a homogenous, infinite waveguide filled with a non-dispersive dielectric, \mathbf{B} and \mathbf{D} can be rewritten as

$$\mathbf{B} = \mu \mathbf{H}, \quad (3)$$

and

$$\mathbf{D} = \epsilon \mathbf{E}. \quad (4)$$

These constitutive relations can now be used to simplify (1-2) as in

$$\nabla \times \mathbf{E} = -j\omega\mu\mathbf{H}, \quad (5)$$

and

$$\nabla \times \mathbf{H} = -j\omega\epsilon\mathbf{E}. \quad (6)$$

In the case of the infinite waveguide, the TM and TE modes can be fully solving for E_z and H_z respectively as all other field components can be derived from these two transverse fields [2], [3]. With this, (5-6) can be manipulated to solve for two independent 2-dimensional Helmholtz equations as

$$\nabla_t^2 E_z + k_c^2 E_z = 0 \quad \text{on } \Omega, \quad (7)$$

and

$$\nabla_t^2 H_z + k_c^2 H_z = 0 \quad \text{on } \Omega \quad (8)$$

where $\nabla_t^2 = \partial_x^2 + \partial_y^2$ the the trasverse Laplacian operator in cartesian coordinates, $k_c^2 = \omega^2\mu\epsilon - k_z^2$ is the cutoff wave number, k_z is the wavenumber in the direction of propagation, and Ω denotes all non-boundary locations within the simulation domain.

These relations hold for all locations excluding those on the PEC walls of the waveguide. This PEC wall condition manifests in the form of a Dirichlet boundary condition

$$E_z = 0 \quad \text{on } \partial\Omega \quad (9)$$

for the TM mode and Neumann boundary conditions

$$\partial_x H_z = 0, \quad \partial_y H_z = 0 \quad \text{on } \partial\Omega \quad (10)$$

for the TE mode where $\partial\Omega$ denotes the PEC surface surrounding the waveguide.

2) *Galerkin Weak Formulation:* With the governing equations established, we can now proceed with the discretization of an arbitrarily shaped waveguide to solve for both the transverse electric and magnetic fields. Using FEM, we break these 2D waveguide slices into a finite set of finitely sized elements and approximate the solution of (7-8) over each element. Triangular elements are chosen as they can be meshed together to form the boundaries of arbitrarily curved shapes making them ideal for modeling geometries with no analytic solutions [3]. Linearly interpolating functions are used to approximate the solution of (7-8) at the nodes of each element. Linear interpolating functions are chosen for their overall simplicity and adequate accuracy for the determination of waveguide parameters [2], [3].

For an arbitrary triangular element, an generic scalar field ϕ can be Linearly interpolated over using

$$\phi^{(e)}(x, y) = a + bx + cy \quad (11)$$

where (e) refers to a specific element, a, b, c are scaling constants and x, y are the coordinates of the location within the node [3]. This interpolation scheme can now be applied to find the field value at an arbitrary node on the element as

$$\phi_l^{(e)} = a + bx_l + cy_l \quad (12)$$

where x, y are the coordinates of the node [3]. These nodal field expressions can now be combined to rewrite (11) in terms of the potentials calculated at each node as

$$\phi^{(e)}(x, y) = N_1^{(e)}(x, y)\phi_1^{(e)} + N_2^{(e)}(x, y)\phi_2^{(e)} + N_3^{(e)}(x, y)\phi_3^{(e)} \quad (13)$$

with an arbitrary interpolating function $N_l^{(e)}$ given by

$$N_l^{(e)}(x, y) = \frac{1}{2\Delta^{(e)}} \left(a_l^{(e)} + b_l^{(e)}x + c_l^{(e)}y \right) \quad (14)$$

where $\Delta^{(e)}$ is the area of element e and $a_l^{(e)}, b_l^{(e)}, c_l^{(e)}$ are given by the following as in [3]

$$\begin{aligned} a_1^e &= x_2^e y_3^e - x_3^e y_2^e, b_1^e = y_2^e - y_3^e, c_1^e = x_3^e - x_2^e \\ a_2^e &= x_3^e y_1^e - x_1^e y_3^e, b_2^e = y_3^e - y_1^e, c_2^e = x_1^e - x_3^e \\ a_3^e &= x_1^e y_2^e - x_2^e y_1^e, b_3^e = y_1^e - y_2^e, c_3^e = x_2^e - x_1^e. \end{aligned} \quad (15)$$

With definitions (13-15) an arbitrary field with potential Dirichlet boundary conditions (noted by D) can be expressed as the superposition of all fields at each node as

$$\phi = \sum_{j=1}^N N_j \phi_j + \sum_{j=1}^N N_j^D \phi_j^D \quad (16)$$

With the discretization of a generic field outlined, The Galerkin weak forms of (7-8) will now be derived in parallel. We begin by multiplying (7-8) by a weighting function which is identical to that of an interpolating function for the Galerkin procedure such that $w_i = N_i$. The resulting weak forms are

$$\iint_{\Omega} N_i (\nabla_t^2 E_z + k_c^2 E_z) d\Omega = 0 \quad (17)$$

and

$$\iint_{\Omega} N_i (\nabla_t^2 H_z + k_c^2 H_z) d\Omega = 0. \quad (18)$$

In order for the linear weighting and basis functions N_i, N_j to work well, the laplacian term in 19-20 needs to be "spread-out". To accomplish this, integration by parts is exploited as follows

$$\begin{aligned} \iint_{\Omega} (\nabla_t N_i \cdot \nabla_t E_z - k_c^2 E_z N_i) d\Omega \\ = (N_i (\hat{n} \cdot \nabla_t E_z))_{\partial\Omega} \end{aligned} \quad (19)$$

and

$$\iint_{\Omega} (\nabla_t N_i \cdot \nabla_t H_z - k_c^2 H_z N_i) d\Omega = (N_i(\hat{n} \cdot \nabla_t H_z))_{\partial\Omega} \quad (20)$$

With these forms in hand, we are now able to simplify the right hand sides of (19-20) using the boundary conditions found in (9-10). The right hand side of (19) disappears as E_z is explicitly set to zero on $\partial\Omega$ in the Dirichlet boundary condition (9). Likewise, the right hand side of (20) reduces to zero as the Neumann boundary condition in (10) sets $\nabla_t H_z = 0$. Despite the fact that both right hand sides reduce to zero, there is an important implementation detail that results in the final equations that arises due to the Dirichlet term in (16). For simplicity, this term will be left out of the remaining equations however the impact of the Dirichlet term on (19) will be discussed in Section II-3.

Substituting in the generic field outlined in (16) with the exclusion of the Dirichlet term as previously mentioned results in the following general eigenvalue equations

$$[A]\{E_z\} = k_c^2[B]\{E_z\} \quad (21)$$

and

$$[A]\{H_z\} = k_c^2[B]\{H_z\} \quad (22)$$

to solve for the TM and TE modes respectively where $[A]$ and $[B]$ are sparse coefficient matrices. Individual coefficients in these matrices are calculated as

$$A_{ij} = \iint_{\Omega} (\nabla_t N_i \cdot \nabla_t N_j) d\Omega \quad (23)$$

and

$$B_{ij} = \iint_{\Omega} (N_i N_j) d\Omega. \quad (24)$$

3) Finite Element Matrix Assembly: With the Galerkin weak form of both Helmholtz equations derived, and the general eigenvalue problems established, we are now able to outline the assembly of the matrices $[A]$ and $[B]$. These matrices are constructed using the standard FEM matrix assembly process. Using this procedure, (23-24) are not explicitly calculated in one fell swoop for all (i, j) . Rather, the contributions from each element are accumulated on local nodes (l, k) [3]. This allows for the assembly of the FEM matrices via a simple iteration over all elements without requiring all interactions between adjacent elements to be calculated ahead of time which would be costly. To facilitate this, a given meshing tool needs to provide the physical locations of all nodes as well as a connectivity list relating elements to their corresponding nodes.

Using the assembly process, and the analytical forms of the integrals of (23-24), the contributions of local nodes (l, k) on the global FEM matrices are as follows

$$A_{lk} = \frac{b_l^{(e)} b_k^{(e)} + c_l^{(e)} c_k^{(e)}}{4\Delta^{(e)}}, \quad (25)$$

and

$$B_{lk} = \frac{\Delta^{(e)}(1 + \delta_{lk})}{12} \quad (26)$$

where δ_{lk} is the Kronecker delta function which is the mathematical representation of the ternary statement: " $\delta_{lk} = 1$ if $(l==k)$: 0;".

With the procedure for assembling the FEM matrices outlined, it is now important to note the differences between $[A]$ and $[B]$ between the TM and TE modes. When solving the TM modes using 21, $[A]$ and $[B]$ contain nodes on $\partial\Omega$ as they are unknown. Thus $[A]$ and $[B]$ are both of size $n \times n$ where n is the number of nodes in the geometry. On the other hand, when solving for the TE mode using (22), nodes on $\partial\Omega$ are set to 0, as per the Dirichlet boundary condition, thus do not explicitly contribute to $[A]$ and $[B]$. As such, these matrices are both of size $(n - b) \times (n - b)$ where b is the number of nodes on the boundary.

III. NUMERICAL RESULTS

With the mathematical model now fully established we now proceed to discuss the implementation of this model in Section III-A. From here Section III-B verifies the model against exact dispersion relations for multiple modes in rectangular waveguides. Section III-C performs an analysis of Dispersion characteristics in circular waveguides and addresses the advantages of using FEA for this task. Finally, Section III-D compares the dispersion characteristics of the rectangular and ridged rectangular waveguides for multiple modes and discusses practical applications of ridged waveguides.

A. Implementation

All meshes used in the following sections were generated using Coreform Cubit [4] with a tutorial provided by [2]. For the rectangular waveguide found in III-B, a WR-90, X-band waveguide with $a = 0.02286\text{m}$ and $b = 0.01016\text{m}$ was used [5]. For the circular waveguide used in III-C, a similarly sized circular waveguide of radius $r = 0.01\text{m}$ was used. In order to compare the non-ridged to the ridged waveguide the same WR-90, X-band waveguide was used in Section III-D as in Section III-B however with two $0.0025 \times 0.0025\text{m}$ notches cut out along the long edge. Example meshes of the later two geometries can be found in Figures 1-2. These meshes were generated using Coreform Cubit's TriAdvance algorithm all containing ≈ 2000 nodes which is appropriate for the applications studied here. Coreform Cubit's `nodeset` feature was used to create a set of all nodes on the boundaries of these geometries. This allows for $O(1)$ lookups of elements on the boundary which was utilized heavily when performing TE mode analysis. These meshes were saved into the ANSYS `.inp` ASCII format which was chosen as it is human readable which was invaluable during the development of this code.

The mathematical model outlined in Section II was implemented in Python for its general flexibility and existing numerical packages such as NumPy and SciPy which were used to solve the general eigenvalue problems established in (22-21). In addition to these packages, the MeshIO package

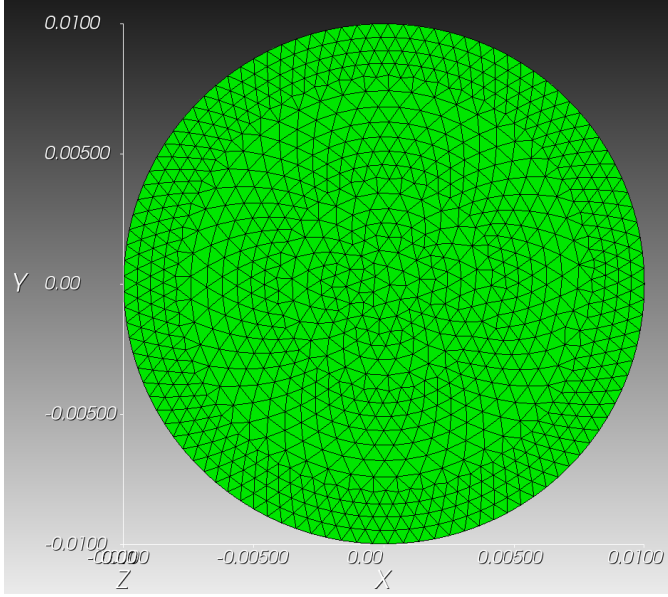


Fig. 1: Circular Waveguide Mesh used in Section III-C

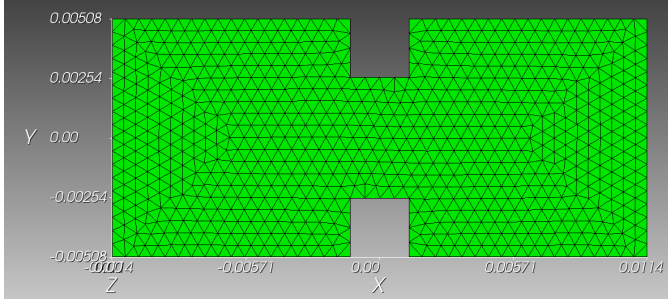


Fig. 2: Ridged Rectangular Waveguide Mesh used in Section III-D

was used as it has a built in reader for `.inp` files allowing mesh data to be read in with ease. From this, all generated data was directly plotted using Matplotlib thereby eliminating the need to save any generated data to disk.

B. Verification and Validation

Prior to performing any kind of ‘novel’ analysis, the implemented model must first be benchmarked against analytic results. For this reason, we will first consider the case of a WR-90, X-band waveguide WR-90, X-band waveguide with $a = 0.02286\text{m}$ and $b = 0.01016\text{m}$ [5].

In this and all following sections the spatial distributions of TE modes will be plotted. Only one mode will be plotted per section as these are merely visual aids in comparison to the dispersion charts which will contain data from the first 3 TE and TM modes. The choice of the given TE mode is entirely arbitrary and was chosen for its post processing simplicity and to ensure adequate comparisons exist in the literature [1]. The TE_{11} , H_z field distribution can be found in Fig. 3.

As seen in Fig. 3 the TE_{11} , H_z field profile matches that of the TE_{11} found in the literature thus confirming its accuracy in recreating spatial field profiles. The TE_{10} and TE_{21} modes

profiles were also vetted however are not shown here to reduce clutter.

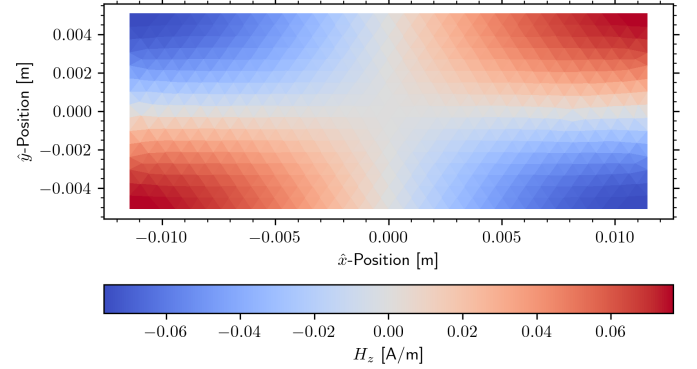


Fig. 3: TE_{11} , H_z Field Distribution in a Rectangular WR-90, X-band Waveguide

Next, a dispersion plot of the first three TE and TM modes in this waveguide is constructed. To benchmark to theory, the following analytic cutoff wave number is used

$$k_c = \sqrt{\left(\frac{m\pi}{a}\right)^2 + \left(\frac{n\pi}{b}\right)^2} \quad (27)$$

where m and n are the corresponding mode propagation numbers. From this, the first three, unique and nonzero simulated cutoff wave numbers from both the TE and TM modes were used to create the dispersion plot in Fig. 4.

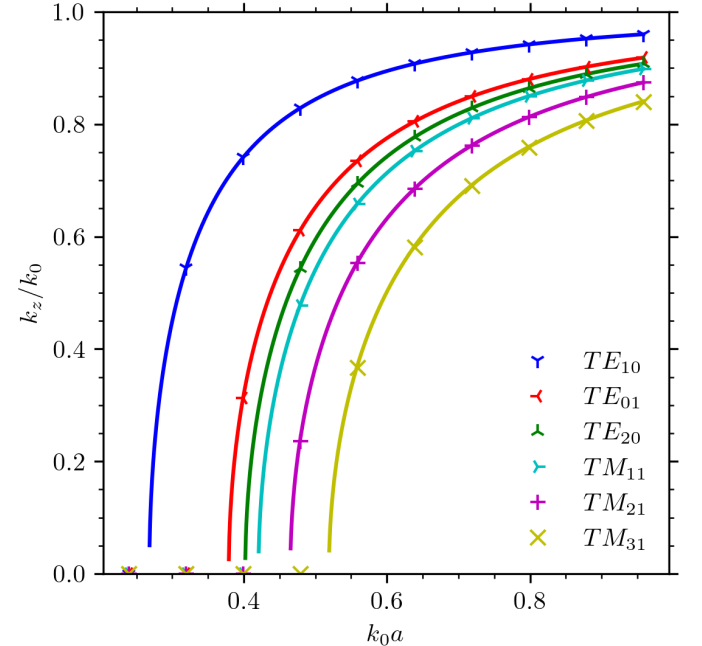


Fig. 4: Dispersion Plots of First Three TE and TM Modes in Rectangular WR-90, X-band Waveguide with Solid Lines as Analytical Results and Corresponding Markers as Simulated Results

As seen in Fig. 4, the dispersion relations predicted by the implemented model match that predicted by theory excellently. Additionally, this demonstrates that the choice of using ≈ 2000

nodes to represent these geometries is more than sufficient to ensure convergence on the true solution. With this, we move on to assess more sophisticated waveguides knowing that the underlying mathematical model is sound.

C. Circular Waveguides

With the model successfully validated against the analytic results of a rectangular waveguide, we now move to assess a circular waveguide of radius $r = 0.01\text{m}$. We first perform one last visual verification step by comparing the field profiles of the TE_{01} and TE_{11} modes generated by our model to that of the analytic profiles found in literature. The simulated TE_{01} H_z profile can be found in Fig. 5.

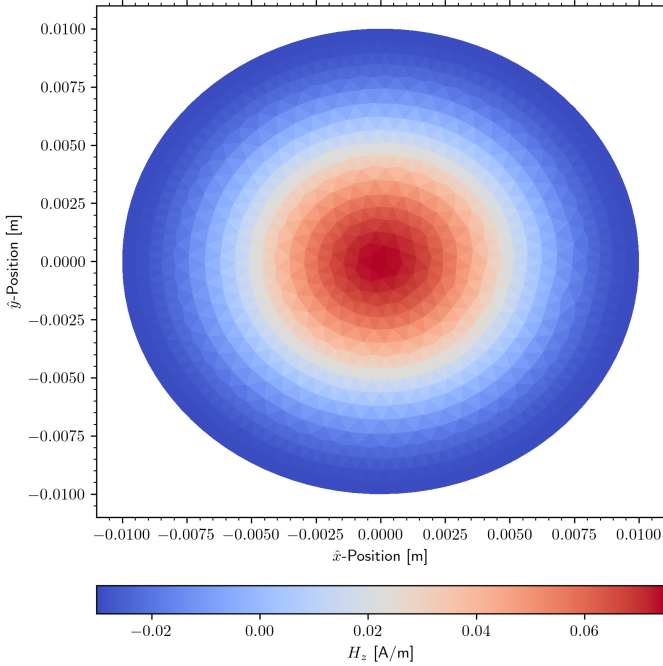


Fig. 5: TE_{01} , H_z Field Distribution in a Circular Waveguide with $r = 0.01\text{m}$

As seen in Fig. 5 the H_z profile matches that found in the literature [1] thereby providing additional validation for the implemented numerical model. These field plots also highlight one of the main strengths of FEM which is its ability to work with unstructured grids out of the box. Modeling a similar profile using a finite difference method would result in egregious stair-stepping error if performed in Cartesian coordinates or would require a special derivation in polar or cylindrical coordinates which could limit the model's usefulness. On the other hand, FEA is able to handle these curved geometries using unstructured grids with relative ease.

From here we perform a similar analysis to that of Fig. 4 for circular waveguides. Traditionally, producing such plots would require tables containing roots of the Bessel function of the first kind p_{nm} and its derivative p'_{nm} which are used to determine the cutoff wave numbers as

$$k_c = \frac{p'_{nm}}{r}, \quad (28)$$

and

$$k_c = \frac{p_{nm}}{r} \quad (29)$$

respectfully for the TE and TM modes. Using the above FEM, we are able to directly calculate the dispersion relations for any circular waveguide without the use of the roots of a Bessel function or its derivative. The simulated dispersion relations can be found in Fig. 6.

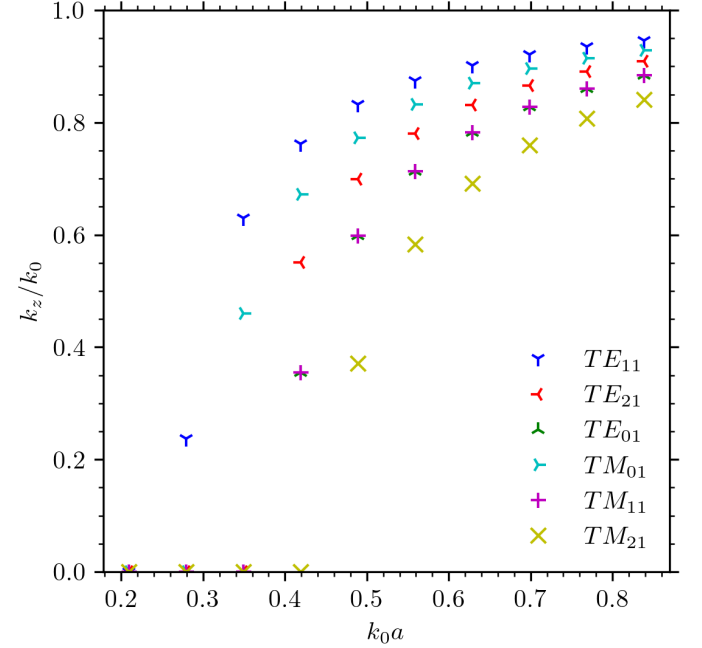


Fig. 6: Dispersion Plots of First Three TE and TM Modes in a Circular Waveguide with $r = 0.01\text{m}$

As seen in Fig. 6, the bandwidth between individual propagation modes in a circular waveguide is much less than that of rectangular waveguides as documented in Fig. 4. This is perhaps most notable between the TE_{11} dominant mode and the next TM_{01} mode which is rather small. This is well documented in the literature [6] and is one of the main factors limiting circular waveguides from being used in wide-band applications. Finally, FEA was able to successfully predict the equivalence of the cutoff wave number for the TE_{01} and TM_{11} modes which is well documented in the literature [1] thereby providing one last verification step prior to considering ridged rectangular waveguides.

D. Comparison of Ridged and Non-Ridged Waveguides

With all validation steps completed, we now focus on the comparison of a standard WR-90, X-band waveguide to that of a double ridged WR-90, X-band waveguide. As seen in Fig. 2 ridges are of size $0.0025 \times 0.0025\text{m}$ and are placed at the centerline of the waveguide. Similarly to Section III-B, we first consider the H_z field profile of the TE_{11} mode as shown in Fig. ??.

As seen in Fig. ?? the field profile is nearly identical to that of the non-ridged WR-90 waveguide shown in Fig. ?. This is expected as the propagation mode is identical

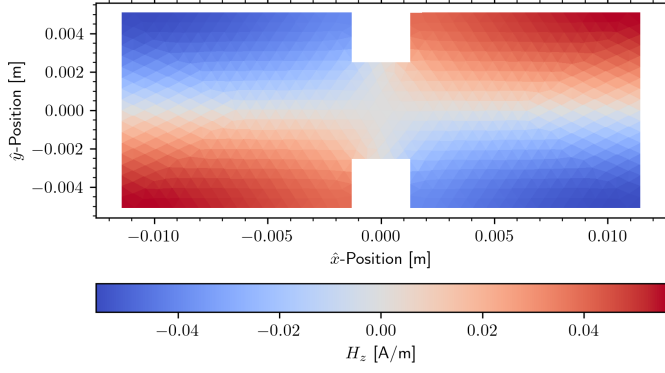


Fig. 7: TE_{11} , H_z Field Distribution in a Ridged Rectangular WR-90, X-band Waveguide

despite the introduction of ridges. To demonstrate differences we now look to creating a dispersion plot for this ridged waveguide. To demonstrate differences between the ridged and base waveguides, we plot the theoretical base dispersion curves as solid lines, and the corresponding simulated data for the same modes as markers. Said plot can be found in Fig. 8.

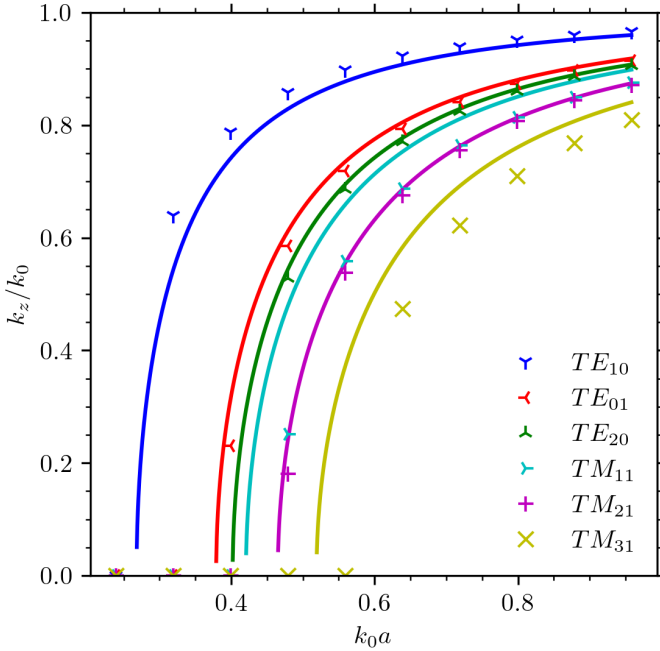


Fig. 8: TE_{11} , H_z Field Distribution in a Ridged Rectangular WR-90, X-band Waveguide with Solid Lines as the Theoretical Dispersion Relation for Base Waveguide and Corresponding Markers as Simulated Dispersion Relation for Ridged Waveguide

It is clear from fig 8 that the cutoff wave number of the dominant TE_{10} mode is less than that of the rectangular waveguide in alignment with the theory [1]. In addition to this, all fields with cutoff wave numbers greater than the dominant mode all experience an increase in cutoff wave number within the ridged waveguide. These phenomenon can all be explained via field buckling caused by the inclusion of ridges. To demonstrate this, the field profiles of the dominant

TE_{10} modes for both the base and ridged waveguides can be found in Figs. 9-10.

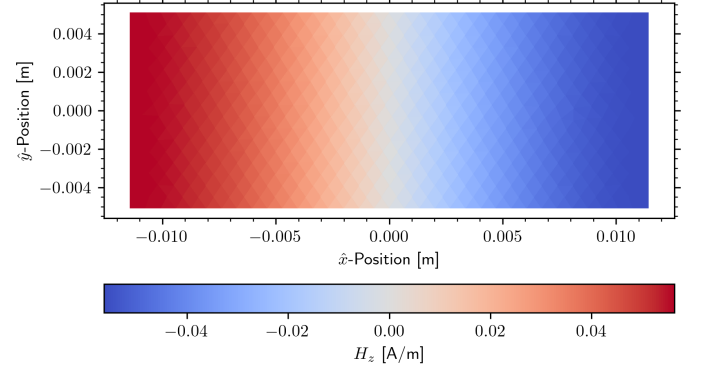


Fig. 9: Dominant TE_{10} , H_z Field Distribution in a Rectangular WR-90, X-band Waveguide

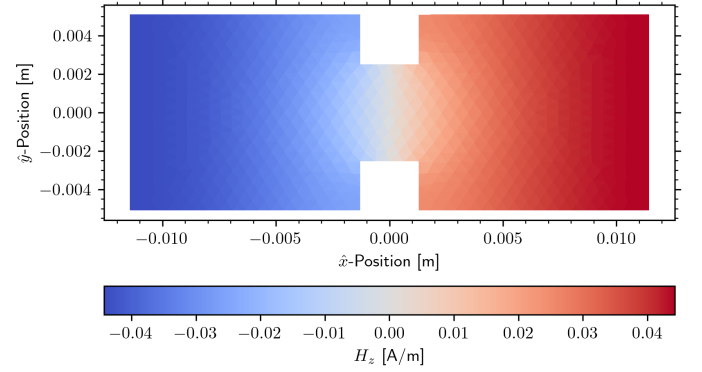


Fig. 10: Dominant TE_{10} , H_z Field Distribution in a Ridged Rectangular WR-90, X-band Waveguide

Figure 9 shows that in the base waveguide there are two distinct regions within the H_z field profile. In the case of the ridged waveguide, the ridges align with the gap between these field regions allowing for the same field profile to be achieved at lower frequencies thus resulting in the lowering of the cutoff wave number. In other words, the inclusion of ridges facilitates a lower overall field buckling for this propagation mode. In contrast to this, higher order modes such as the TE_{11} mode found in Fig. 7 require increased buckling in order to satisfy the boundary conditions of (9-10) to achieve the same field profile. This increased field buckling directly corresponds to an increase in the minimum cutoff wave number, and corresponding frequency content, to recreate these higher-order, more complex, propagation modes.

For this reason, ridged waveguides offer superior bandwidth for the dominant modes making them superior for transmitting high-bandwidth signals.

IV. CONCLUSION

A 2-dimensional finite element method program was developed from Maxwell's Equations allowing for field distribution and dispersion analysis of arbitrarily shaped homogenous

waveguides. The model was first validated against the analytic field profiles and dispersion curves for a rectangular waveguide. From here, additional verification was performed on the field profiles of circular waveguides. From here, the model was used to predict the dispersion characteristics of said circular guide which can be difficult to do analytically without tabulated Bessel function data. Finally, the model was used to compare ridged waveguides to their non-ridged counterparts. It was shown that the inclusion of ridges significantly expands the bandwidth available to the dominant TE_{10} mode in alignment with theory. This phenomenon was explained using the change in field buckling caused by complex modes requiring higher frequencies to achieve the same field profiles where as the buckling working in the favor of simpler field profiles resulting in a lowering of the cutoff wave number.

While relatively general in the sense that the model works for any .inp input waveguide mesh, the model would benefit from increased work regarding the identification of modes which currently is done manually by the user in order to produce dispersion curves and field profile plots. In addition

to this, it would be interesting to combine this model with the FDTD model developed in the last project in order to generate the field profiles of more complex waveguides for use in the TF/SF source condition. This would allow for temporal analysis of more sophisticated waveguides than the simple rectangular model used in the former project.

REFERENCES

- [1] D. M. Pozar, *Microwave Engineering*. John Wiley & Sons, 2011.
- [2] T. E. Roth, *ECE 61800 Lecture Notes*. Purdue University, 2024.
- [3] J.-M. Jin, *Theory and Computation of Electromagnetic Fields*. John Wiley & Sons, 2011.
- [4] Coreform LLC, "Coreform cubit," <https://coreform.com/products/coreform-cubit/>, 2024, [Online; accessed 26-March-2024].
- [5] Everything RF contributors, "Rectangular waveguide sizes," <https://www.everythingrf.com/tech-resources/waveguides-sizes>, 2021, [Online; accessed 28-February-2024].
- [6] Cadence System Analysis, "An introduction to circular waveguide modes," <https://resources.system-analysis.cadence.com/blog/msa2021-an-introduction-to-circular-waveguide-modes>, [Online; accessed 27-March-2024].